Int. J. Heat Mass Transfer. Vol. 25, No. 9, pp. 1363–1376, 1982
Printed in Great Britain

0017-9310/82/091363-14 $03.00/0
Pergamon Press Ltd.

EFFECTS OF WALL RADIATION AND CONDUCTION ON THE STABILITY OF A FLUID IN A FINITE SLOT HEATED FROM BELOW

D. W. HATFIELD
Chemical, Nuclear, and Thermal Engineering Department, University of California, Los Angeles, CA 90024, U.S.A.

and

D. K. EDWARDS
Department of Mechanical Engineering, University of California, Irvine, CA 92717, U.S.A.

(*Received* 2 *April* 1982)

Abstract—Critical Rayleigh number is found for a fluid bounded by vertical parallel walls of finite height. The thermally expansive, radiatively diathermanous fluid is heated from below and cooled from above at rigid ends. The ends have arbitrary but equal emissivity. The vertical walls are thin and conducting, have arbitrary uniform emissivity, and are adiabatic on their exterior surfaces. Effects of aspect ratio, side wall conductance, and side and end wall emissivities on critical Rayleigh number are found analytically with the Galerkin technique and confirmed experimentally with holographic interferometry.

NOMENCLATURE

a, wavenumber;
A, area;
A, B, C, D, E, F, coefficients;
b, $\pi D/L$;
c, even beam function;
D, distance between sidewalls;
$\hat{e}_x, \hat{e}_y, \hat{e}_z$, unit vectors;
$\mathbf{f}$, velocity trial function;
g, acceleration of gravity;
G, irradiation;
H, dimensionless conduction number;
i, j, k, l, integers;
I, integral;
k, thermal conductivity;
K, shape factor kernel;
L, distance between hot and cold plates;
N, summation limit;
M, matrix element;
n, complex number;
N_D, radiation–conduction number, $(4\sigma T_m^3 D)/k$;
Nu, Nusselt number at $x = 0$ and y-averaged;
p, perturbation in pressure;
P, pressure;
Pr, Prandtl number, ν/α;
q, heat flux or transcendental root;
Ra_D, Rayleigh number, $g\beta\Delta T D^4/\nu\alpha L$;
s, odd beam function;
S, irradiation integral;
t, thickness or time;
T, temperature;
$\mathbf{u}, \mathbf{v}$, velocity;
V, volume;
W, distance between sidewalls, $W \gg D$;
$x, y, z, \bar{z}$, spatial coordinates.

Greek symbols

α, thermal diffusivity;
β, volume expansion coefficient;
γ, perturbation in irradiation;
ΔT, temperature difference between horizontal plates;
ε, emissivity;
θ, dimensionless temperature;
λ, transcendental root;
μ, dynamic viscosity or transcendental root;
ν, kinematic viscosity;
π_i, trial function;
ρ, density;
σ, Stefan–Boltzmann constant;
τ, trial function;
ϕ, perturbation in θ;
ψ, trial function.

Subscripts

c, critical value;
C, cold plate;
D, based on length D;
H, hot plate;
i, j, k, l, summation integers;
m, mean value or evaluated at mean temperature;
L, based on length L;
0, base flow state;
r, radiation;
w, wall;
x, at $x = \pm 0.5$;
y, at $y = \pm 0.5\, W/D$.

Superscripts

*, complex conjugate or effect of radiation on base flow neglected;
derivative or dummy variable.

1. INTRODUCTION

THE PREDICTION of the onset of motion in a right rectangular cylinder of height L and of large horizontal aspect ratio W/D is considered. For example, the thermal designer may wish to size a rectangular honeycomb to suppress convection in a Francia type solar collector [1, 2].

Wooding [3] treated 3-dim. convective disturbances in a fluid bounded by two parallel rigid vertical walls and by shear-free top, bottom and ends when the fluid was subject to a destabilizing vertical temperature gradient. He found that the critical Rayleigh number based on wall spacing D depends on horizontal and vertical wavenumbers when the walls are adiabatic and is π^4 when the walls are perfectly conducting. Edwards [4] showed that if the walls are arbitrarily conducting in a finwise manner, the critical Rayleigh number is a function of two wavenumbers and the dimensionless quantity $H = k_w t_w/(kD)$ where k_w is the wall conductivity, t_w is the wall thickness, and k is the fluid conductivity. The analysis was extended [5] to include the slot whose walls conduct arbitrarily and exchange radiant energy through a diathermanous fluid. The wall radiative exchange, like wall conduction, stabilizes the fluid from convective disturbances by adding thermal damping.

To account for the rigid top and bottom, Edwards and Sun [5] suggested using the infinite slot solution and adjusting the vertical wavenumber. Davis [6] and Catton [7 9] derived the critical Rayleigh number for a radiation-opaque fluid without recourse to an adjusted wavenumber approximation by applying the Galerkin technique.

Experimental data on the onset of motion and heat transfer after instability have been reported for radiation-opaque silicone-oil-filled slots [10, 11] and radiation-transparent air-filled slots [12, 13]. The results of Smart, Hollands, and Raithby [13] indicate that the emissivity of the top and bottom enclosure surfaces, which is not accounted for in existing theory [5], has a significant effect on the critical Rayleigh number.

The objective of the investigation reported in this paper was to apply the Galerkin technique to determine the critical Rayleigh number for the finite slot filled with a diathermanous fluid and having arbitrarily finwise-conducting vertical walls and arbitrary vertical and horizontal wall emissivity. The present analysis incorporates the effect of the radiation on the temperature and velocity fields in the fluid before instability. Experimental data for air-filled slots obtained by holographic interferometry are also reported.

2. FORMULATION OF PROBLEM

Initially a thermally-expansive and radiation-transparent fluid fills a finite slot (finite L/D and infinite W/D) as shown in Fig. 1. The upper horizontal boundary is isothermal at T_C, the lower horizontal boundary is isothermal at higher temperature T_H, and

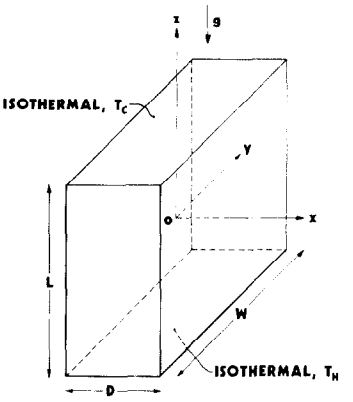

FIG. 1. Cell geometry and coordinate system.

the vertical walls (sidewalls) conduct isotropically and partially reflect thermal radiation diffusely. Due to radiative exchange between the sidewalls of the slot, the vertical temperature variation is not linear, as would be the case when radiation heat transfer is absent or the sidewalls are infinitely conducting. Thus a weak 2-dim. base-flow convection occurs. For a Boussinesq fluid, the base flow temperature and velocity fields in the fluid are governed by the dimensionless equations

$$\nabla \cdot \mathbf{v}_0 = 0, \tag{1}$$

$$\nabla^2 \mathbf{v}_0 - \nabla P_0 + Ra_D(L/D)\theta_0 \hat{e}_z - Pr^{-1}\mathbf{v}_0 \cdot \nabla \mathbf{v}_0 = 0, \tag{2}$$

$$\nabla^2 \theta_0 - \mathbf{v}_0 \cdot \nabla \theta_0 + (D/L)\mathbf{v}_0 \cdot \hat{e}_z = 0 \tag{3}$$

where $\mathbf{v}_0$, θ_0, and P_0 are the velocity, temperature deviation from linearity, and pressure measured in units of α/D, ΔT, and $(\alpha\mu)/D^2$, respectively. The coordinates are measured in units of lateral distance D; Pr is the Prandtl number; and the Rayleigh number based on D is

$$Ra_D = (g\beta\Delta T D^4)/\nu\alpha L.$$

The boundary conditions on velocity are

$$\mathbf{v}_0 = 0 \text{ on } x = \pm\frac{1}{2} \text{ and } z = \pm\frac{1}{2}\frac{L}{D}.$$

The temperature is subject to

$$\theta_0 = 0 \quad \text{on} \quad z = \pm\frac{1}{2}\frac{L}{D}$$

and, assuming that the sidewalls are insulated on the exterior and thin enough to justify the fin approximation,

$$H\left(\frac{\partial^2\theta_0}{\partial y^2} + \frac{\partial^2\theta_0}{\partial z^2}\right) = \pm\frac{\partial\theta_0}{\partial x} + q_{r0} \text{ on } x = \pm\frac{1}{2} \tag{4}$$

where $H = (k_w t_w)/(kD)$ and q_{r0} is the net radiation flux out of the wall, measured in units of $4\sigma T_m^3 \Delta T$. When $\Delta T \ll T_m$ as required by the Boussinesq approxi-

mation, the radiation flux can be expressed in linearized form

$$q_{r0} \doteq \varepsilon_x N_D(\theta_0 - G_0) \tag{5}$$

where ε_x is the emissivity of the sidewalls ($x = \pm 0.5$), $N_D = (4\sigma T_m^3 D)/k$ is a radiation–conduction parameter, and G_0 is the dimensionless irradiation flux indicated by the integro-equation

$$G_0 = \int_A [\varepsilon' \theta_0' + (1 - \varepsilon')G_0' + (D/L)(z - z')]K \mathrm{d}A' \tag{6}$$

where K is the shape factor kernel between differential wall areas $\mathrm{d}A$ and $\mathrm{d}A'$. The horizontal walls are assumed to have equal (diffuse) emissivity ε_z and specular reflectivity $1 - \varepsilon_z$ in order to simplify the evaluation of G_0.

Small, 3-dim. Bernard-type convective disturbances from the base flow state are assumed, and second-order terms are neglected. At marginal stability (see Appendix) the perturbations in velocity, temperature, and pressure, $\mathbf{u}$, ϕ, and p, respectively, are governed by

$$\nabla \cdot \mathbf{u} = 0, \tag{7}$$

$$\nabla^2 \mathbf{u} - \nabla p + Ra_D(L/D)\phi \hat{e}_z - Pr^{-1} \nabla \cdot \mathbf{u}\mathbf{v}_0 = 0, \tag{8}$$

$$\nabla^2 \phi + (D/L)\mathbf{u} \cdot \hat{e}_z - \mathbf{v}_0 \cdot \nabla \phi - \mathbf{u} \cdot \nabla \theta_0 = 0. \tag{9}$$

The boundary conditions are

$$\mathbf{u} = 0 \quad \text{on } x = \pm \frac{1}{2} \quad \text{and } z = \pm \frac{1}{2}\frac{L}{D}$$

$$\phi = 0 \quad \text{on } z = \pm \frac{1}{2}\frac{L}{D}$$

and

$$H\left(\frac{\partial^2 \phi}{\partial y^2} + \frac{\partial^2 \phi}{\partial z^2}\right) = \pm \frac{\partial \phi}{\partial x} + q_r \quad \text{on } x = \pm \frac{1}{2} \tag{10}$$

where

$$q_r = \varepsilon_x N_D(\phi - \gamma) \tag{11}$$

and

$$\gamma = G - G_0 = \int_A [\varepsilon' \phi' + (1 - \varepsilon')\gamma']K \mathrm{d}A'. \tag{12}$$

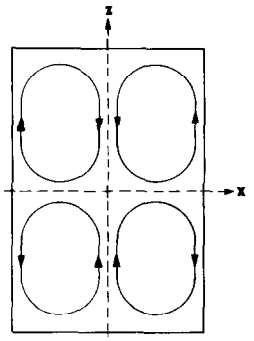

FIG. 2. Schematic of base flow velocity field.

Equations (7)–(9), subject to the boundary conditions, and the base flow solution $\mathbf{v}_0$ and θ_0 constitute an eigenvalue problem for the Rayleigh number. The lowest positive Ra_D which satisfies the equations is the critical Rayleigh number, $Ra_{D,c}$.

3. METHOD OF SOLUTION

The base flow and thermal stability eigenvalue problems formulated in the previous section are solved by the Galerkin technique (e.g. [14]).

Base flow

The base flow velocity, temperature, and pressure are approximated by

$$\mathbf{v}_0 \doteq \sum_{i=1}^{N} A_{0i}\, \mathbf{f}_{0i}(x, z),$$

$$\theta_0 \doteq \sum_{i=1}^{N} [B_{0i}\tau_{0i}(x, z) + C_{0i}\psi_{0i}(x, z)],$$

$$P_0 \doteq \sum_{i=1}^{N} F_{0i}\pi_{0i}(x, z)$$

where A_{0i}, B_{0i}, C_{0i}, and F_{0i} are unknown coefficients and $\mathbf{f}_{0i}$, τ_{0i}, ψ_{0i}, and π_{0i} are trial functions which have sufficient freedom to resemble the variable being approximated.

For the velocity field there were chosen trial functions $\mathbf{f}_{0i}$ which satisfy continuity and the no-slip boundary conditions, that is

$$\mathbf{f}_{0i} = -\frac{D}{L} s_i(x) s_i'\left(\frac{D}{L} z\right)\hat{e}_x + s_i'(x) s_i\left(\frac{D}{L} z\right)\hat{e}_z$$

where

$$s_i(x) = \frac{\sinh(\mu_i x)}{\sinh(\mu_i/2)} - \frac{\sin(\mu_i x)}{\sin(\mu_i/2)}$$

are the odd series of beam functions. The roots μ_i are selected to make the derivatives, $s_i'(x)$, equal zero at $x = \pm 0.5$ and are tabulated in ref. [15]. A schematic of the base flow velocity field being approximated is shown in Fig. 2.

The mixed Galerkin method [14] is employed in the temperature field approximation, since neither the energy equation (3) nor the sidewall boundary conditions (4)–(6) can be satisfied by the chosen trial functions. Hence, one set of functions, τ_{0i}, selected so that each satisfies the 2-dim. Laplace equation, are employed in the solution to the boundary conditions, and another set of functions, ψ_{0i}, each of which satisfies the homogeneous sidewall boundary conditions approximately are used in the solution to the momentum and energy equations, equations (2) and (3). Suitable functions are

$$\tau_{0i} = \cosh[2\pi i(D/L)x] \sin[2\pi i(D/L)z](L/D),$$

$$\psi_{0i} = \cos[\pi q_{0i} x] \sin[2\pi i(D/L)z](L/D)$$

where fractional coefficients q_{0i} are determined so that

each function ψ_{0i} satisfies the homogeneous sidewall boundary conditions in a Galerkin manner. Specification of π_{0i} is not necessary.

The unknown coefficients in the variable expansions are determined by substituting the expansions into the appropriate differential equations or boundary conditions and forcing the resultant errors to be orthogonal to the trial functions over the domain of the independent variables [14]. The resulting Galerkin orthogonality relations for equations (4), (2) and (3) are, respectively,

$$\sum_{i=1}^{N} B_{0i}\{[4\pi^2 i^2 (D/L)^2 H + 2\pi i (D/L)\tanh(\pi i D/L) + \varepsilon_x N_D]\delta_{ij} - \varepsilon_x N_D E_{0ij}\} = \varepsilon_x N_D D_{0j}, \quad (13)$$

$$\sum_{i=1}^{N} \{A_{0i} M_{011ij} + C_{0i} Ra_D M_{012ij}\} = -Ra_D \sum_{k=1}^{N} B_{0k} M_{013jk} + Pr^{-1} \sum_{k=1}^{N}\sum_{l=1}^{N} A_{0k} A_{0l} M_{014jkl}, \quad (14)$$

$$\sum_{i=1}^{N} \{A_{0i}[M_{021ij} - \sum_{k=1}^{N} B_{0k} M_{022ijk}] + C_{0i} M_{023ij}\} = \sum_{k=1}^{N}\sum_{l=1}^{N} A_{0l} C_{0k} M_{024jkl}, \quad (15)$$

$$j = 1, \ldots, N$$

where the matrix elements in equations (14) and (15) are volume integrals as follows:

$$M_{011ij} = \int_V \mathbf{f}_{0j} \cdot \nabla^2 \mathbf{f}_{0i}\, dV,$$

$$M_{012ij} = \int_V \mathbf{f}_{0j} \cdot \hat{e}_z \psi_{0i}\, dV,$$

$$M_{013jk} = \int_V \mathbf{f}_{0j} \cdot \hat{e}_z \tau_{0k}\, dV,$$

$$M_{014jkl} = \int_V \mathbf{f}_{0j} \cdot (\nabla \cdot \mathbf{f}_{0k}\mathbf{f}_{0l})\, dV,$$

$$M_{021ij} = \int_V \mathbf{f}_{0i} \cdot \hat{e}_z \psi_{0j}\, dV,$$

$$M_{022ijk} = \int_V \psi_{0j} \mathbf{f}_{0i} \cdot \nabla \tau_{0k}\, dV,$$

$$M_{023ij} = \int_V \psi_{0j} \nabla^2 \psi_{0i}\, dV,$$

$$M_{024jkl} = \int_V \psi_{0i} \mathbf{f}_{0k} \cdot \nabla \psi_{0j}\, dV,$$

and where E_{0ij} and D_{0j} in equation (13) are the solutions to the linear equations

$$\sum_{k=1}^{N} E_{0ik}[\delta_{kl} - (1 - \varepsilon_x) S_{21k}] = \varepsilon_x S_{21i}, \quad (16)$$

$$\sum_{k=1}^{N} D_{0k}[\delta_{kl} - (1 - \varepsilon_x) S_{21k}] = S_{31}, \quad (17)$$

$$i, l = 1, \ldots, N$$

and

$$S_{21k} = 2(D/L) \int_{-0.5L/D}^{0.5L/D} \times \int_A \sin[2\pi l (D/L) z] \sin[2\pi k (D/L) z'] K dA' dz \quad (18)$$

$$S_{31} = 2(D/L) \int_{-0.5L/D}^{0.5L/D} \times \int_A \sin[2\pi l (D/L) z] (z - z') K dA' dz. \quad (19)$$

The last four expressions arise from the Galerkin solution to the integro-equation (6). The matrix volume integrals ($-0.5 \leqslant x \leqslant 0.5$ and $-0.5L/D \leqslant z \leqslant 0.5L/D$) are evaluated analytically, and integrals containing the pressure vanish due to the solenoidal nature of the velocity trial functions.

The values of q_{0i} in the ψ_{0i} trial functions are the roots to the transcendental equation

$$4\pi^2 i^2 (D/L)^2 H + \varepsilon_x N_D (1 - E_{0ii}) - \pi q_{0i} \tan(q_{0i}\pi/2) = 0 \quad (20)$$

$$0 \leqslant q_{01} \leqslant 1, \quad 2 \leqslant q_{02} \leqslant 3, \text{ etc.}$$

Perturbation equations

The solution to equations (8) and (9) are approximated by

$$u \doteq \sum_{i=1}^{N} A_i \mathbf{f}_i(x, y, z),$$

$$\phi \doteq \sum_{i=1}^{N} B_i \tau_i(x, y, z),$$

$$p \doteq \sum_{i=1}^{N} F_i \pi_i(x, y, z)$$

where $\mathbf{f}_i$ satisfy continuity and the no-slip conditions and τ_i satisfy the boundary conditions approximately.

As shown by refs. [6–9] the most unstable mode of convection is rolls whose x-component of velocity is essentially zero. The velocity variation in y is periodic with wavenumber a. Suitable velocity trial functions are

$$\mathbf{f}_i = -\frac{D}{L}\frac{\lambda_i}{a}\cos[(2i-1)\pi x] \sin(ay) c_i'[(D/L)z]\hat{e}_y + \cos[(2i-1)\pi x]\cos(ay) c_i[(D/L)z]\hat{e}_z$$

where

$$c_i(x) = \frac{\cosh(\lambda_i x)}{\cosh(\lambda_i/2)} - \frac{\cos(\lambda_i x)}{\cos(\lambda_i/2)}$$

are the even series of beam functions and λ_i are selected

so that the derivatives, $c_i'(x)$, are zero at $x = \pm 0.5$.

The temperature trial functions, which should have the same vertical symmetry as the vertical velocity component, are

$$\tau_i = \cos(\pi q_i x)\cos(ay)\cos[(2i-1)\pi(D/L)z](L/D).$$

The coefficients q_i, analogous to q_{0i}, are evaluated so that equations (10)–(12) are satisfied approximately, that is

$$[a^2 + \pi^2(2i-1)^2(D/L)^2]H + \varepsilon_x N_D(1 - E_{ii}) - \pi q_i \tan(q_i\pi/2) = 0 \quad (21)$$

$$0 \leqslant q_1 \leqslant 1, \quad 2 \leqslant q_2 \leqslant 3, \text{ etc.}$$

where E_{ii} are obtained from

$$\sum_{k=1}^{N} E_{ik}[\delta_{kl} - (1 - \varepsilon_x)S_{1lk}] = \varepsilon_x S_{1li} \quad (22)$$

$$l = 1, \ldots, N$$

and

$$S_{1li} = \left\{ \int_{-a/2}^{a/2} \int_{-0.5L/D}^{0.5L/D} \int_A \cos(ay)\cos(ay')\cos[(2i-1) \times \pi(D/L)z]\cos[(2l-1)\pi(D/L)z']K\,dA'\,dy\,dz \right\} \times \left\{ \int_{-a/2}^{a/2} \int_{-0.5L/D}^{0.5L/D} \cos^2(ay)\cos^2[(2i-1) \times \pi(D/L)z]\,dy\,dz \right\}. \quad (23)$$

The latter two equations arise from the Galerkin solution to the integro-equation (12).

The Galerkin orthogonality relations associated with the momentum and energy equations, equations (8) and (9), are

$$\sum_{i=1}^{N} (A_i M_{11ij} + Ra_D B_i M_{12ij}) = 0, \quad (24)$$

$$\sum_{i=1}^{N} (A_i M_{21ij} + B_i M_{22ij}) = 0, \quad (25)$$

$$j = 1, \ldots, N.$$

The matrix elements are

$$M_{11ij} = \int_V \mathbf{f}_j \cdot \nabla^2 \mathbf{f}_i dV - Pr^{-1} \sum_{k=1}^{N} A_{0k} \int_V \mathbf{f}_j \cdot (\nabla \cdot \mathbf{f}_i \mathbf{f}_{0k}) dV,$$

$$M_{12ij} = \int_V \mathbf{f}_j \cdot \hat{e}_z \tau_i dV,$$

$$M_{21ij} = \int_V \mathbf{f}_i \cdot \hat{e}_z \tau_j dV - \sum_{k=1}^{N} B_{0k} \int_V \tau_j \mathbf{f}_i \cdot \nabla \tau_{0k} dV - \sum_{k=1}^{N} C_{0k} \int_V \tau_j \mathbf{f}_i \cdot \nabla \psi_{0k} dV,$$

$$M_{22ij} = \int_V \tau_j \nabla^2 \tau_i dV - \sum_{k=1}^{N} A_{0k} \int_V \tau_j \mathbf{f}_{0k} \cdot \nabla \tau_i dV.$$

The volume integrations are over $-0.5 \leqslant x \leqslant 0.5$, $-0.5a \leqslant y \leqslant 0.5a$, and $-0.5L/D \leqslant z \leqslant 0.5L/D$.

Equations (24) and (25) have a non-trivial solution (nonzero A_i and B_i) only if the determinate of the $2N \times 2N$ matrix is zero, that is

$$\det \begin{vmatrix} M_{11ij} & Ra_D M_{12ij} \\ M_{21ij} & M_{22ij} \end{vmatrix} = 0, \quad (26)$$

$$i, j = 1, \ldots, N.$$

The lowest root Ra_D which satisfies this condition is the critical Rayleigh number. It is noted that Ra_D also appears implicitly in M_{11ij}, M_{21ij} and M_{22ij} via the base flow solution, i.e. A_{0k}, B_{0k}, and C_{0k} coefficients.

The base flow temperature and velocity and critical Rayleigh number were determined from the above equations by standard matrix inversion and nonlinear-root-extraction techniques. In order to interpret the results values of $Ra_{D,c}$ were also obtained for the special cases of (1) no base-flow convection (A_{0k} and C_{0k} set to zero) and (2) no base-flow convection or radiation (A_{0k}, B_{0k}, and C_{0k} set to zero). Further details on the numerical procedures including the evaluation of the irradiation integrals S_{1ij}, S_{2ij}, and S_{3i} are given in ref. [16].

4. DESCRIPTION OF EXPERIMENT

Interferometer

The holographic interferometer is essentially that described in ref. [17]. Coherent light (0.633 μm) from a 15 mW Spectra-Physics helium–neon laser is split into an object beam and a reference beam by a variable-silvered mirror, and each beam is expanded to a 100 mm diameter planar wave via a $\times 40$ microscope objective and collimating lens. Pinholes of 5 μm diameter are located at the focal points of the microscope objectives in order to eliminate intensity variations in the wavefronts. The two wavefronts intersect at a Kodak 120-02 photographic plate (here at an angle of 26°) and produce a hologram when the photographic emulsion is exposed simultaneously to the two beams and then developed *in situ*. The reconstructed object beam wavefront, which is recorded when the temperature inside the test section is uniform, and the real-time object beam wavefront, which is distorted by a non uniform temperature field inside the test section, are focused by an achromat lens and interfere to produce an interferogram on Kodak Tri-X film. The interferometer components are mounted to a 1.2 by 3.0 m vibration-isolated optical table.

Test cell

The test cell is constructed of two 10.2 $\times$ 30.6 cm and 0.95 cm thick aluminum plates which are separated by Bakelite spacers (Fig. 3) and are aligned horizontally on the optical table so that the object beam is parallel to the long axis of the cell. The lower plate is electrically heated, and the upper plate is cooled to just above the dew point. The plates were either polished ($\varepsilon_z \doteq 0.1$) or painted black ($\varepsilon_z \doteq 0.9$).

Sidewall partitions, which form 11 side-by-side cells between the aluminum plates, are supported in

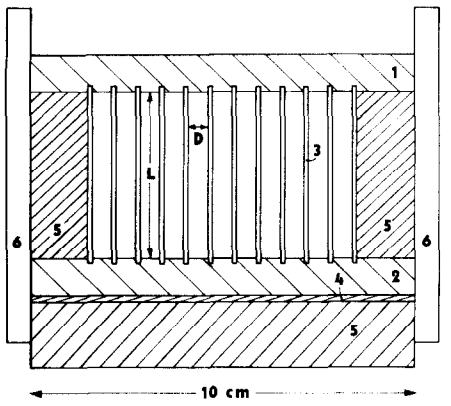

FIG. 3. Test cell cross section, 1 cold aluminum plate, 2 hot aluminum plate, 3 sidewall partitions, 4 electrical heater, 5 insulation, 6 spacers.

0.79 mm wide and 1.27 mm deep milled slots, 6.73 mm apart, in each plate along the long axis of the test cell. The partitions were fabricated from either 0.51 mm thick first-surface aluminized paper ($\varepsilon_x = 0.03$, $k_{wx} = 0.47 \pm 0.02$ W m^{-1} K^{-1}) or a 0.76 mm thick paper-phenolic laminate ($\varepsilon_x \doteq 0.9$, $k_{wx} = 0.69 \pm 0.03$ W m^{-1} K^{-1}). In addition some runs were made with aluminized paper which was painted black.

The ends of the test cell ($y = \pm 0.5\,W/D$) were aluminized paper (untouched or painted black) backed on the exterior with 1.91 cm foam. The ends were lifted up approx. 2 s prior to recording an interferogram.

Table 1 contains a list of the cell characteristics investigated. Subscripts C and H denote the upper cold and lower hot plate, respectively, to allow for unequal plate emissivities. In each case the length of the test section W was 30.6 cm.

Independent measurements of the aluminum plate temperatures were made with chromel–constantan thermocouples inserted in four drilled holes in each plate.

Data reduction

Real-time infinite fringe and finite fringe interferograms were recorded for the seven test-cells described above for the temperature difference range $10 < \Delta T < 40$°C. The mean temperature of the air in the cell was kept near 290 ± 2 K. Between seven and eleven data points (ΔT) were obtained for each cell.

The extraction of the temperature field, averaged in y, from the interferograms was done by standard techniques [16, 18]. The experimental data were plotted as a Nusselt number (dimensionless vertical temperature gradient at $x = 0$, averaged in y, and at $z = \pm 0.5L/D$) vs the Rayleigh number based on lateral distance D. Fluid properties were evaluated at the mean temperature.

Error analysis [16] indicated 5% uncertainty in the experimental Nusselt and Rayleigh numbers.

5. RESULTS AND DISCUSSION

Base flow numerical results

To illustrate the effect of wall radiation on the base flow temperature field, Fig. 4 shows how the dimensionless temperature $T_0 = \theta_0 - zD/L$ varies with the rescaled vertical coordinate $z = zD/L$ at $x = 0$ (centerline) and $x = \pm 0.5$ (sidewalls). In the figure the diagonal straight line corresponds to the temperature variation, at all x, when the sidewall radiant exchange is suppressed or if the sidewalls are perfectly conducting. Characteristics of the temperature field include relatively steep vertical gradients near the horizontal plates, a reduction of the vertical gradient in the fluid core ($x = \bar{z} = 0$) compared to that if there were only conduction and small horizontal temperature differences in the fluid, which drive a base flow convection pattern as indicated in Fig. 2. These effects are due to the sidewall radiative exchange which tends toward a uniform temperature on the sidewalls; that is, in the absence of all conduction and when ε_z or L/D is small, the sidewalls are isothermal, and temperature jumps occur at each end. Vertical conduction in the fluid and walls and the endwall radiative transfer for finite L/D and ε_z oppose this tendency.

The vertical temperature gradient at $x = \bar{z} = 0$ is listed in Table 2 as a function of L/D, H, and ε_z for $\varepsilon_x = 1$. The temperature deviation from a linear vertical profile is most pronounced when the sidewall emissivity ε_x is high, the endwall emissivity ε_z is low, the wall conduction parameter H is low, and the radiation–conduction parameter is high. Other parameters fixed, the radiation effects on the fluid and sidewall temperature are maximized at a certain aspect ratio L/D. For instance, the results in Table 2 indicate that the minimum slope $-\partial T/\partial \bar{z}(0,0)$ occurs for a L/D between 4 and 8 when $\varepsilon_x = 1$, $\varepsilon_z = 0$, $H = 0.03$, and $N_D = 4$.

Table 1. Cell characteristics

Cell	L (mm)	D (mm)	L/D	W/L	H	ε_x	ε_y	ε_{zC}	ε_{zH}	N_D
1	24.9	6.22	4.00	12.2	0.76	0.03	0.03	0.1	0.1	1.39
2	24.7	6.17	4.00	12.3	0.76	0.9	0.03	0.1	0.1	1.38
3	24.7	6.17	4.00	12.3	0.76	0.9	0.9	0.1	0.1	1.38
4	24.7	6.17	4.00	12.3	0.76	0.9	0.03	0.9	0.9	1.38
5	43.2	5.97	7.234	7.06	1.70	0.9	0.03	0.1	0.1	1.33
6	43.2	5.97	7.234	7.06	1.70	0.9	0.03	0.9	0.1	1.33
7	43.2	5.97	7.234	7.06	1.70	0.9	0.03	0.9	0.9	1.33

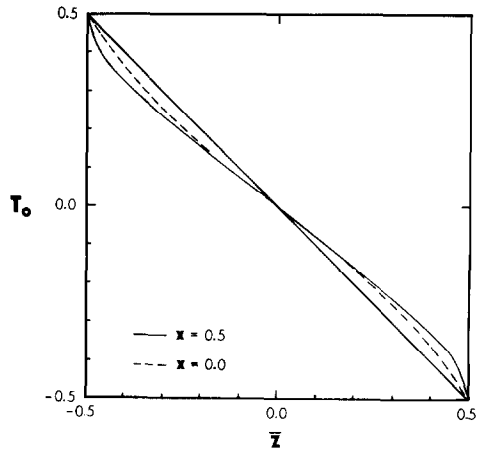

FIG. 4. Base flow vertical temperature variation, $L/D = 4$, $\varepsilon_x = 1$, $H = 0$, and $N_D = 5$.

Table 2 also contains values of the magnitude of the maximum base flow velocity, $v_{0,\max}$, which occurs near $x = 0$ and $\bar{z} = \pm 0.2$. To convert these numbers to dimensional values, the $v_{0,\max}$ are multiplied by α/D. For air at room temperature and $D = 0.5$ cm, $\alpha/D = 0.35\ \text{cm s}^{-1}$. It is noted that the velocity field induced by sidewall radiant exchange is quite small in most of the cases considered in this investigation.

Critical Rayleigh number numerical results

The critical Rayleigh number was computed from equation (26) by 3- and 5-term Galerkin approximations. The 3-term values were essentially converged, since the 3- and 5-term calculations differed only in the fourth significant digit. In fact, 1-term Galerkin solutions are fairly good approximations to the converged solutions.

Table 2. Base-flow state, $\varepsilon_x = 1.0$ and $N_D = 4.0$

L/D	H	ε_z	$-\partial T/\partial \bar{z}(0, 0)$	$v_{0,\max}$
2	0.03	0.0	0.74	0.245
4	0.03	0.0	0.57	0.079
4	0.30	0.0	0.65	0.064
4	0.03	1.0	0.80	0.029
4	0.30	1.0	0.83	0.026
6	0.03	0.0	0.55	0.031
8	0.03	0.0	0.57	0.014

Table 3. Critical Rayleigh numbers

L/D	a/b	H	ε_x	ε_z	N_D	$Ra_{D,c}$	$Ra^*_{D,c}$
2	1.1	0.03	0			287.0	287.0
2	1.1	0.03	1	0	1	362.8	332.3
2	1.2	0.03	1	0	4	529.1	414.0
2	1.1	0.03	1	1	1	351.0	334.6
2	1.2	0.03	1	1	4	471.5	417.3
4	1.1	0.03	0			45.6	45.6
4	1.1	0.03	1	0	1	79.8	67.3
4	1.3	0.03	1	0	4	173.7	112.5
4	1.1	0.03	1	1	1	74.7	68.8
4	1.3	0.03	1	1	4	137.0	114.8
4	1.1	0.10	0			51.1	51.1
4	1.1	0.10	1	0	1	83.6	71.9
4	1.3	0.10	1	0	4	171.8	115.2
4	1.1	0.10	1	1	1	79.0	73.3
4	1.3	0.10	1	1	4	138.7	117.4
4	1.1	0.30	0			65.5	65.5
4	1.1	0.30	1	0	1	94.2	84.0
4	1.3	0.30	1	0	4	169.9	122.5
4	1.1	0.30	1	1	1	90.4	85.3
4	1.3	0.30	1	1	4	143.6	124.5
4	1.1	1.00	0			105.0	105.0
4	1.2	1.00	1	0	1	124.3	116.8
4	1.3	1.00	1	0	4	174.9	142.8
4	1.2	1.00	1	1	1	121.4	117.5
4	1.3	1.00	1	1	4	158.8	144.3
6	1.1	0.03	0			18.1	18.1
6	1.1	0.03	1	0	1	38.4	31.5
6	1.3	0.03	1	0	4	99.8	62.9
6	1.1	0.03	1	1	1	35.6	32.5
6	1.3	0.03	1	1	4	77.1	64.7
8	1.1	0.03	0			9.73	9.73
8	1.1	0.03	1	0	1	23.5	19.1
8	1.2	0.03	1	0	4	66.2	42.5
8	1.1	0.03	1	1	1	21.7	19.7
8	1.3	0.03	1	1	4	51.9	44.0

In Table 3 there are listed values of $Ra_{D,c}$ evaluated by a 3-term expansion and with simplification number (1) described in section 3, that is, with base-flow convection neglected. Spot checks on $Ra_{D,c}$ computed with and without this simplification indicate agreement to 1% for $L/D = 2$ and 0.3% for $L/D \geqslant 4$.

The ratio a/b, where a is the horizontal wavenumber and $b \equiv \pi D/L$, specifies the shape of the rolls at instability. If $a/b = 1$ the rolls are square, and if $a/b > 1$ the width of the rolls is less than the height. The value taken on by a/b is that which minimizes the critical Rayleigh number (Fig. 5). The ratios a/b indicated in Table 3 are within ± 0.05 of the values that minimize $Ra_{D,c}$. In the limit of adiabatic walls (H and ε_x zero) and large L/D, square rolls ($a = b$) minimize $Ra_{D,c}$. As indicated in the table, the influence of wall conduction, radiation and finite L/D is to require $a_{min} > b$; that is, the higher buoyant energy per unit of sidewall area associated with low width-to-height rolls is necessary to balance the additional dissipative effects due to endwall shear and wall conduction and radiation.

Table 3 also contains values of the critical Rayleigh number, denoted $Ra^*_{D,c}$, evaluated with simplification number (2), that is, with neglect of both convection and radiation upon the base state temperature. The discrepancies between $Ra_{D,c}$ and $Ra^*_{D,c}$ in the table indicate that the simplification is not justified; however, the $Ra^*_{D,c}$ values are useful in distinguishing between (1) the effects of predominantly transverse (y-direction) sidewall radiative exchange in damping out thermal perturbations in the fluid and (2) the influence of the axial (z-direction) radiative exchange on the temperature field before instability. For instance, consider the case $L/D = 4$ and $H = 0.10$. When radiation effects are absent, $Ra_{D,c}$ is 51. When $\varepsilon_x = 1$, $\varepsilon_z = 0$, and $N_D = 4$ the critical Rayleigh number is increased by 237% to 172. For reference, $Ra^*_{D,c} = 115$. Part of the 237% increase in $Ra_{D,c}$, let us say $(115-51)/51 = 125\%$, is due to the stabilizing effect of transverse sidewall radiation in damping out thermal perturbations in the fluid, and the remainder, an additional 112% is due to the influence of axial sidewall radiation on the base flow temperature field.

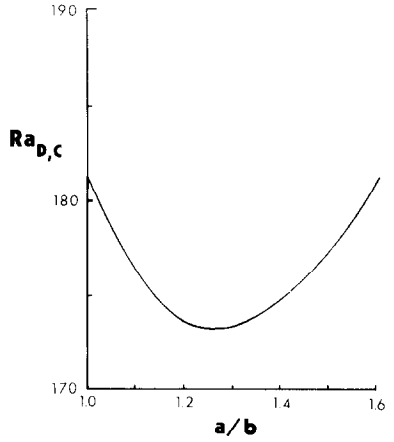

FIG. 5. Critical Rayleigh number vs ratio a/b. $L/D = 4$, $\varepsilon_x = 1$, $\varepsilon_z = 0$, $H = 0.03$, and $N_D = 4$.

The numerical results indicate that the combined effect of transverse and axial sidewall radiant exchange in the finite slot always stabilizes the fluid from the growth of small disturbances. Highest stabilization occurs when N_D is high, the sidewalls are black, and the endwalls are non-emitting, that is, when the axial endwall radiation is low. Increasing the endwall emissivity destabilizes the fluid. Since $Ra_{D,c}$, but not $Ra^*_{D,c}$, is influenced significantly by ε_z, it is apparent that the destabilizing effect of endwall emissivity is due to the influence of axial endwall radiation in steepening the base flow temperature gradient in the center of the slot (see also Table 2).

The combined action of wall conduction and radiation is complex, since in some circumstances the critical Rayleigh number $Ra_{D,c}$ can first decrease upon increasing H from zero, pass through a minimum, and then increase with further wall conduction. An example of this behavior in Table 3 is the case $L/D = 4$, $\varepsilon_x = 1$, $\varepsilon_z = 0$, and $N_D = 4$ with parameter $H = 0.03$, 0.10, 0.30 and 1.00. In the absence of radiation, wall conduction always stabilizes the fluid [4, 9]. Hence, with strong radiation coupling, the destabilizing influence of increasing wall conduction at low H is due to axial wall conduction counteracting the axial sidewall radiative coupling on the base flow vertical temperature gradient in the fluid core.

Experimental results

Figures 6–8 show typical infinite fringe interferograms recorded with cells 7, 1 and 2, respectively. Each fringe is the locus of equal optical path length through the test cell and, hence, are isotherms averaged in the y-direction. The temperature difference between consecutive fringes is 2.3°C at $T_{mean} = 300$ K. At other temperatures the ΔT/fringe goes like $(T/T_{mean})^2$. In the present study accurate results could be obtained with the infinite fringe technique for $\Delta T \geqslant 25$°C. For lower ΔT it was found to be advantageous to use the finite fringe technique [16], but the interferograms are not shown here, since the infinite fringe interferograms are better suited to illustrate the qualitative features of the temperature field inside the test cells.

In Fig. 6, variations in the temperature field over the 11 cells are indicated. This figure demonstrates that edge effects influence only the two outermost cells; the central cells are free of edge effects.

The interferograms in Fig. 7 depict the isotherms in cell 1 in which radiation effects are small ($\varepsilon_x = 0.03$ and $\varepsilon_{zC} = \varepsilon_{zH} = 0.1$). In Fig. 7(a) the Rayleigh number is just above the critical value as indicated by the nearly uniform fringe spacing, and the heat transfer is mainly conductive. At higher Ra_D in Figs. 7(b)–(d), Benard cellular convection in the form of multiple rolls with axes in the x-direction, is characterized by fringes which are widely spaced in the central regions of the cells where convectional transport dominates and which are narrowly spaced near the horizontal boun-

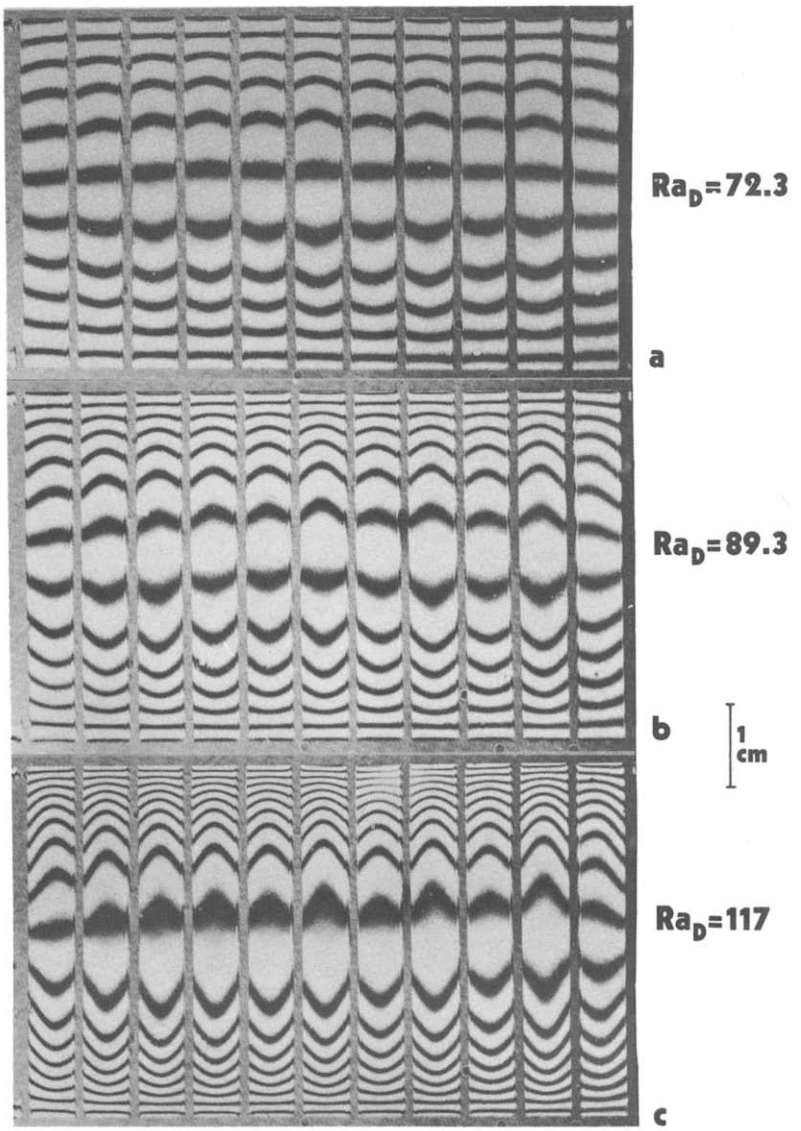

FIG. 6. Interferograms, cell 7 (see Table 1).

daries where conductional transport dominates. Note also that the fringes are curved, indicating horizontal temperature differences, due to sidewall conduction.

Figure 8 shows interferograms for cell 2 which is identical to cell 1 except that the sidewalls have high emissivity. In Fig. 8(a) the Rayleigh number is close to $Ra_{D,c}$; the influence of sidewall radiation on the base flow temperature field is apparent in the curvature and relatively close spacing of the fringes near the horizontal plates. After instability, Figs. 8(b)–(d), the temperature fields are qualitatively similar to those in Fig. 7. If a comparison is made at a particular Ra_D, e.g. Figs. 7(c) and 8(c), the suppression of convection due to sidewall radiative exchange can be seen in the fringe spacing; in Fig. 7(c) the spacing near the centers of the cells is somewhat greater than that in Fig. 8(c).

The data reduction for the finite fringe interferograms involved determining the variation of temperature with $\bar{z}$ at $x = 0$ and plotting the dimensionless negative vertical temperature gradient at $\bar{z} = \pm 0.5$, or Nusselt number, vs the Rayleigh number. For the finite fringe interferograms it was not necessary to obtain T vs $\bar{z}$ data since the vertical temperature gradients could be obtained directly from interferograms. Figures 9–11 show Nu vs Ra_D plots for cells 1–7. The solid lines are curve fits through the data points. The intersection of two curves, one through low (before stability) and the other through high (after instability) Ra_D data, fixes the experimental critical Rayleigh number. These numbers are tabulated in Table 4. Note that for cell 6, in which the plates have different emissivities, the Nusselt numbers evaluated at $\bar{z} = \pm 0.5$ are not the same, because the higher radiative flux at the high emissivity end requires a lower conductive heat flux and vice versa. The curve intersections indicate approximately the same value of critical Rayleigh number, however.

The influence of sidewall emissivity on $Ra_{D,c}$ for L/D

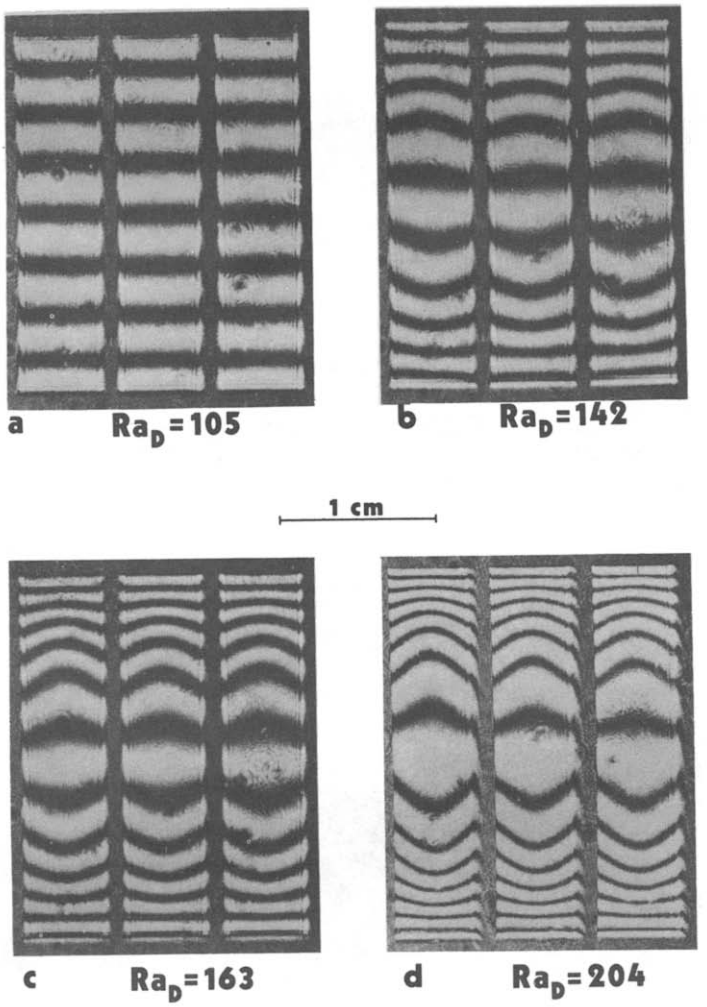

FIG. 7. Interferograms, cell 1 (see Table 1).

$= 4, H = 0.76, N_D = 1.4$, and low endwall emissivity is seen by comparing the results for cells, 1, 2, and 3 in Table 4. When $\varepsilon_x = \varepsilon_y = 0.03$, $Ra_{D,c} = 98$. As the emissivity of the long sidewall, ε_x, is increased to 0.9 the critical Rayleigh number is augmented by 29%, and, if in addition the emissivity of the short sidewall, ε_y, is increased to 0.9, there is a further 8% increase in $Ra_{D,c}$. As theory predicts, there is a slight decrease in $Ra_{D,c}$ when the endwall emissivity is increased (cell 4).

The data for cells 5–7 show that the critical Rayleigh number for the slot with unequal plate emissivities lies between the values for slots with two low emissivity plates or with two high emissivity plates. This result was also reported by Smart *et al.* [13] for the slot with low emissivity top and high emissivity bottom plates.

Comparison of numerical and experimental results

The experimental critical Rayleigh numbers are compared to 3-term Galerkin $Ra_{D,c}$ calculations in Table 4. Also listed is the percentage difference between the two values. In all but one case the numerical analysis slightly underpredicts the critical Rayleigh number. The worst case of 9% difference is for cell 3 in which $\varepsilon_y = 0.9$, for which the slot analysis has no provision. Conducting and radiating walls at $y = 0.5W/D$ would be expected to have a stabilizing influence on $Ra_{D,c}$ as indicated by the experimental results.

Additional comparisons are made in Table 5 in which the 5-term Galerkin numerical and experimental values of the base flow vertical temperature gradient at $\bar{z} = -0.5, 0.0$, and 0.5 are listed. The values agree to within 5% except for one case in which the deviation is 9%.

The numerical critical Rayleigh number calculations are compared to the experimental data of Smart *et al.* [13] in Table 6. In that study the authors determined $Ra_{D,c}$ from calorimetric Nusselt vs Rayleigh number heat transfer data for air-filled, high horizontal aspect ratio ($W/D = 44$), multiple-communicating cells. For set ups 1, 2 and 3 the sidewall partitions were constructed of polyethylene film which was significantly transparent to thermal radiation. However, the authors noted that, because of symmetri-

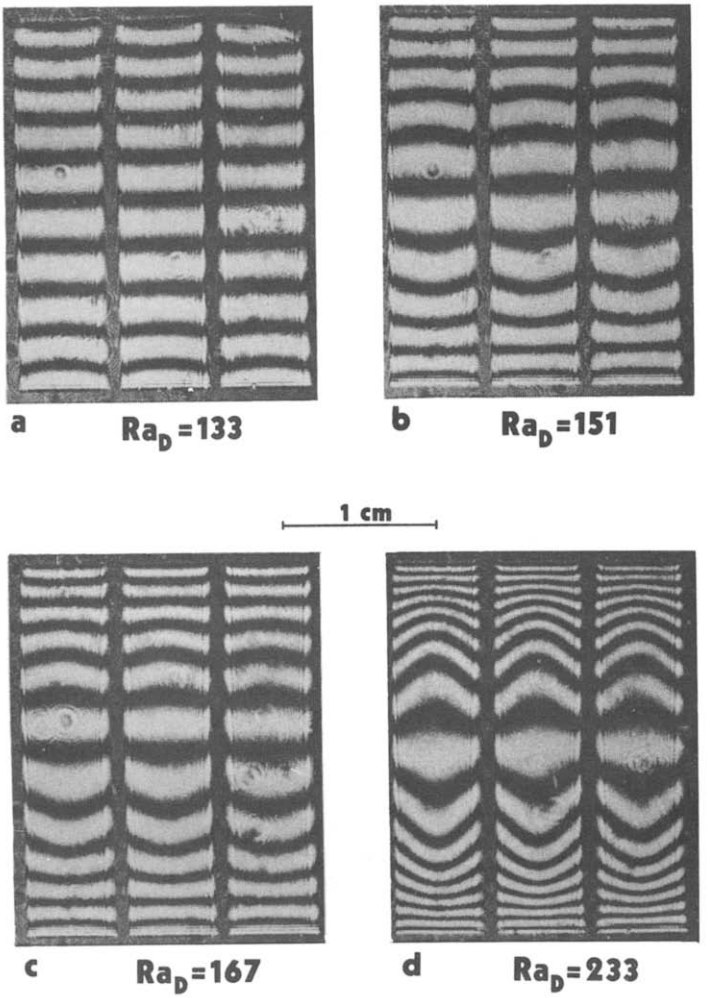

FIG. 8. Interferograms, cell 2 (see Table 1).

cal convective motions in adjacent cells, the sidewalls can be treated as having an effective specular reflectivity equal to $1-\varepsilon_x$. The sidewall partitions for set ups 4, 5 and 6 were radiation-opaque.

For set ups 1, 2 and 3 the experimental and numerical results differ by no more than 12% even though the sidewalls are assumed to be diffuse in the analysis. When the sidewall emissivity is high and endwall emissivity is low, the predicted critical Rayleigh number agrees well with experiment; however, if the endwall emissivities are high the present Galerkin solutions overpredict $Ra_{D,c}$ by 17%.

6. SUMMARY

The main results of the study are as follows:

(1) Sidewall and endwall radiation in the finite slot

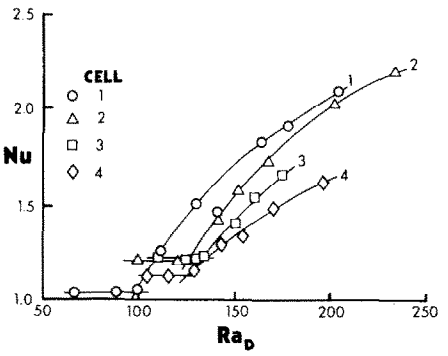

FIG. 9. Nusselt number at $x = 0$ vs Rayleigh number, cells 1–4.

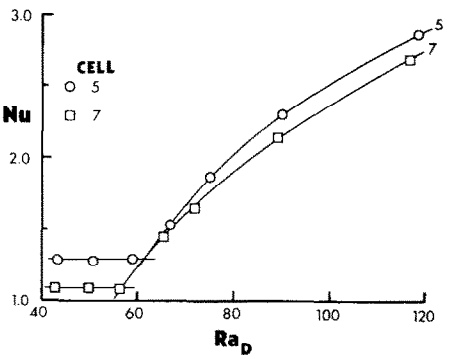

FIG. 10. Nusselt number at $x = 0$ vs Rayleigh number, cells 5 and 7.

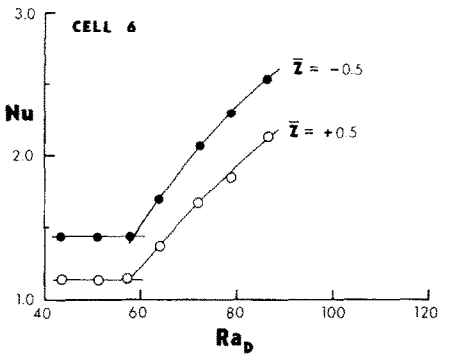

FIG. 11. Nusselt number at $x = 0$ vs Rayleigh number, cell 6.

enclosure affects the critical Rayleigh number by essentially two separate mechanisms:

(a) Axial radiation influences the base flow temperature distribution in the fluid before instability.

(b) Transverse thermal perturbations in the fluid are damped by radiative exchange between sidewall elements adjacent to the perturbed hot and cold fluid regions. High sidewall emissivity is stabilizing in both these mechanisms while high endwall emissivity acts to destabilize in the first mechanism.

(2) Sidewall radiant exchange in the finite slot stabilizes the fluid, and, in the absence of radiation effects, wall conduction stabilizes the fluid as well. However, when both radiation and wall conduction effects are important it is possible for wall conduction to be destabilizing at low values of the wall conduction parameter. This behavior is due to the opposing tendencies of sidewall radiation and conduction on the base flow temperature field.

(3) The numerical predictions agree with present and previous experimental data to within 12% except for one data point.

Acknowledgments—The work reported here was supported in part by the National Science Foundation under grants ENG-75-22936 and ENG-78-25273. Computing was subsidized by the Office of Academic Computing at UCLA.

REFERENCES

1. G. Francia, A new collector of solar radiant energy—Theory and experimental verification, UN Con-

Table 4. Experimental critical Rayleigh numbers

Cell	L/D	H	N_D	ε_x, ε_y, ε_{zC}, ε_{zH}	Exp.	$Ra_{D,c}$ Num.	% Diff.
1	4.0	0.76	1.4	0.03, 0.03, 0.1, 0.1	98	95	−3
2	4.0	0.76	1.4	0.9, 0.03, 0.1, 0.1	127	122	−4
3	4.0	0.76	1.4	0.9, 0.9, 0.1, 0.1	135	122	−9
4	4.0	0.76	1.4	0.9, 0.03, 0.9, 0.9	125	118	−6
5	7.2	1.70	1.3	0.9, 0.03, 0.1, 0.1	62	58	−6
6	7.2	1.70	1.3	0.9, 0.03, 0.9, 0.1	59		
7	7.2	1.70	1.3	0.9, 0.03, 0.9, 0.9	57	57	0

Table 5. Experimental and numerical base flow temperature gradients at $x = 0$

Cell	$-\partial T/\partial \bar{z}\|_{\bar{z}=0}$ Exp.	Num.	$-\partial T/\partial \bar{z}\|_{\bar{z}=\pm 0.5}$ Exp.	Num.
1	0.97	0.99	1.05	1.02
2	0.88	0.88	1.21	1.19
3	0.85	0.88	1.24	1.19
4	0.90	0.93	1.13	1.11
5	0.88	0.91	1.30	1.19
6	0.85		1.13, 1.43	
7	0.90	0.95	1.10	1.11

Table 6. Comparison of numerical $Ra_{D,c}$ to Smart *et al.* [13] data

No.	L/D	W/L	H	N_D	ε_x	ε_{zC}	ε_{zH}	Exp.	$Ra_{D,c}$ Num.	% Diff.
1	5	8.8	0.03	3.04	0.11	0.065	0.065	44	48	8
2	10	4.4	0.03	3.04	0.11	0.065	0.065	20	20	0
3	3	15.0	0.03	3.04	0.11	0.065	0.065	107	120	12
4	5	8.8	0.12	3.04	0.9	0.065	0.065	104	102	−2
5	5	8.8	0.12	3.04	0.9	0.065	0.9	83		
6	5	8.8	0.12	3.04	0.9	0.9	0.9	74	87	17

ference on New Sources of Energy, Rome, Italy, Paper F6 (May 1961).
2. H. Buchberg, D. K. Edwards and O. A. Lalude, Design considerations for cellular solar collectors, ASME Paper No. 68-WA/SOL-3 (1968).
3. R. A. Wooding, Instability of a viscous liquid of variable density in a vertical Hele–Shaw cell, *J. Fluid Mech.* **7**, 501–515 (1960).
4. D. K. Edwards, Suppression of cellular convection by lateral walls, *Trans. Am. Soc. Mech. Engrs*, Series C, *J. Heat Transfer* **91**, 145–150 (1969).
5. D. K. Edwards and W. M. Sun, Prediction of the onset of natural convection in rectangular honeycomb structures, Paper 7/62 Int. Solar Energy Society Conf., Melbourne, Australia (1970).
6. S. H. Davis, Convection in a box: linear theory, *J. Fluid Mech.* **30**, 465–478 (1967).
7. I. Catton, Convection in a closed rectangular region: the onset of motion, *Trans. Am. Soc. Mech. Engrs*, Series C, *J. Heat Transfer* **92**, 186–188 (1970).
8. I. Catton, The effect of insulating vertical walls on the onset of motion in a fluid heated from below, *Int. J. Heat Mass Transfer* **15**, 665–672 (1972).
9. I. Catton, Effects of wall conduction on the stability of a fluid in a rectangular region heated from below, *Trans. Am. Soc. Mech. Engrs*, Series C, *J. Heat Transfer* **94**, 446–452 (1972).
10. D. K. Edwards, J. N. Arnold and P. S. Wu, Correlations for natural convection through high L/D rectangular cells, *Trans. Am. Soc. Mech. Engrs*, Series C, *J. Heat Transfer* **101**, 741–743 (1979).
11. D. Q. Le, D. W. Hatfield and D. K. Edwards, Comparison of data with correlations for natural convection through rectangular cells of arbitrary aspect ratio, *Trans. Am. Soc. Mech. Engrs*, Series C, *J. Heat Transfer*, to be published (1982).
12. W. M. Sun, Effect of arbitrary conduction and radiation on free convection in a cylinder, Ph.D. dissertation UCLA (1970).
13. D. R. Smart, K. G. T. Hollands and G. D. Raithby, Free convection heat transfer across rectangular-celled diathermanous honeycombs, *Trans. Am. Soc. Mech. Engrs*, Series C, *J. Heat Transfer* **102**, 75–80 (1980).
14. L. J. Snyder, T. W. Spriggs and W. E. Stewart, Solution of the equations of change by Galerkin's method, *A.I.Ch.E. Jl* **10**, 535–540 (1964).
15. W. H. Reid and D. L. Harris, On orthogonal functions which satisfy four boundary conditions, *Astrophys. J., Suppl. Ser.* **3**, 429–452 (1958).
16. D. W. Hatfield, The effects of wall radiation and conduction on the stability of free convection in a rectangular enclosure heated from below, Ph.D. dissertation, UCLA (1982).
17. D. W. Hatfield and D. K. Edwards, Edge and aspect ratio effects on natural convection from the horizontal heated plate facing downwards, *Int. J. Heat Mass Transfer* **24**, 1019–1024 (1981).
18. M. Hauf and U. Grigull, Optical methods in heat transfer, in *Advances in Heat Transfer* (edited by J. P. Hartnett) Vol. 6. Academic Press, New York (1970).
19. M. Sherman and S. Ostrach, On the principle of exchange of stabilities for the magnetohydrodynamic thermal stability problem in completely confined fluids, *J. Fluid Mech.* **24**, 661–671 (1966).

APPENDIX

THE PRINCIPLE OF EXCHANGE OF INSTABILITIES

Sherman and Ostrach [19] derived a proof of the principle of exchange of instabilities for a completely confined fluid with conducting sidewalls. For the present situation being analyzed the analogs to their equations (20a) and (20b) are

$$\mathrm{Re}(n)(Ra_D I_3 - Pr^{-1} I_4) + I_1 + Ra_D I_2 - Pr^{-1} I_5 = 0 \tag{27}$$

$$\mathrm{Im}(n)\{Ra_D I_3 + Pr^{-1} I_4\} = 0 \tag{28}$$

where n is a complex number in the time dependency factor e^{nt}. The volume integrals are

$$I_1 = \int_V \mathbf{u}^* \cdot \nabla^2 \mathbf{u} \mathrm{d}V,$$

$$I_2 = \frac{L}{D} \int_V [\mathbf{v}_0 \cdot \nabla \phi^* + \mathbf{u}^* \cdot \nabla \theta_0 - \phi \nabla^2 \phi^*] \mathrm{d}V,$$

$$I_3 = \frac{L}{D} \int_V \phi \phi^* \mathrm{d}V,$$

$$I_4 = \int_V \mathbf{u} \cdot \mathbf{u}^* \mathrm{d}V,$$

$$I_5 = \int_V \mathbf{u}^* \cdot (\nabla \cdot \mathbf{u}\mathbf{v}_0) \mathrm{d}V$$

where the asterisk denotes the solution corresponding to the complex conjugate of n, n^*.

If the Rayleigh number is positive, i.e. the fluid is heated from below, equation (28) implies that the imaginary part of n is zero since integrals I_3 and I_4 are positive. Depending on the characteristics of the base flow, $\mathbf{v}_0$ and θ_0, a positive Ra_D may or may not satisfy equation (27). If it does, the critical disturbance is stationary at marginal stability.

EFFET DU RAYONNEMENT A LA PAROI ET DE LA CONDUCTION SUR LA STABILITE D'UN FLUIDE DANS UNE FENTE FINIE CHAUFFEE PAR LE BAS

Résumé—On détermine le nombre de Rayleigh critique pour un fluide limité par des parois parallèles verticales de hauteur finie. Le fluide dilatable, radiant et diathermane est chauffé par le bas et refroidi en haut, sur les extrémités rigides qui ont des émissivités égales mais quelconques. Les parois verticales sont minces et conductrices, elles ont des émissivités uniformes et arbitraires et elles sont adiabatiques à l'extérieur. Les effets du rapport de forme, de la conductance de paroi, des émissivités sur le nombre de Rayleigh critique sont déterminés analytiquement par la technique de Galerkine et sont expérimentalement confirmés par interférométrie holographique.

DIE EINFLÜSSE VON STRAHLUNG UND LEITUNG DER WAND AUF DIE STABILITÄT EINES FLUIDS IN EINEM ENDLICHEN SPALT BEI BEHEIZUNG VON UNTEN

Zusammenfassung—Es wurde eine kritische Rayleigh-Zahl für ein Fluid ermittelt, welches durch senkrechte, parallele Wände von endlicher Höhe begrenzt wird. Das thermisch ausdehnungsfähige, wärmestrahlungsdurchlässige Fluid wird durch Abschlußwände von unten beheizt und von oben gekühlt. Die Abschlußwände haben eine bestimmte gleiche Emissivität. Die vertikalen Wände sind dünn und leitend, haben eine bestimmte gleichmäßige Emissivität und sind an den äußeren Oberflächen adiabat. Die Einflüsse von Seitenverhältnis, Wärmeleitung der Wand und Emissivitäten an den Seiten- und Abschlußwänden auf die kritische Rayleigh-Zahl werden analytisch nach der Galerkin-Methode bestimmt und experimentell durch holografische Interferometrie bestätigt.

ВЛИЯНИЕ ИЗЛУЧЕНИЯ И ТЕПЛОПРОВОДНОСТИ СТЕНКИ НА УСТОЙЧИВОСТЬ ЖИДКОСТИ В НАГРЕВАЕМОЙ СНИЗУ ЩЕЛИ КОНЕЧНЫХ РАЗМЕРОВ

Аннотация—Получено значение критического числа Релея для жидкости, находящейся между вертикальными параллельными стенками конечной высоты. Расширяющаяся при нагревании, пропускающая излучение жидкость подогревается снизу и охлаждается сверху через твердые границы. Они имеют произвольную, но равную излучательную способность. Тонкие и теплопроводные вертикальные стенки имеют произвольную однородную излучательную способность и с внешней стороны теплоизолированы. Методом Галеркина определено влияние геометрического параметра, проводимости боковых стенок и излучательных способностей боковых стенок и торцевых поверхностей на критическое число Релея. Результаты расчетов подтверждены экспериментально с помощью голографической интерферометрии.